Magnetic Resonance Imaging 101 (2023) 25–34

Contents lists available at ScienceDirect

Magnetic Resonance Imaging

journal homepage: www.elsevier.com/locate/mri

Quantitative longitudinal mapping of radiation-treated prostate cancer using MR fingerprinting with radial acquisition and subspace reconstruction

Victoria Y. Yu [a], Ricardo Otazo [a,d], Can Wu [a], Ergys Subashi [a], Manuel Baumann [b], Peter Koken [b], Mariya Doneva [b], Peter Mazurkewitz [b], Daniel Shasha [c], Michael Zelefsky [c], Laura Cervino [a], Ouri Cohen [a,*]

[a] Department of Medical Physics, Memorial Sloan Kettering Cancer Center, New York, NY, USA
[b] Philips Research, MR Research, Hamburg, Germany
[c] Department of Radiation Oncology, Memorial Sloan Kettering Cancer Center, New York, NY, USA
[d] Department of Radiology, Memorial Sloan Kettering Cancer Center, New York, NY, USA

ARTICLE INFO

Keywords:
MR fingerprinting
Prostate cancer
Quantitative parameter mapping
Radiation therapy
Subspace reconstruction

ABSTRACT

MR fingerprinting (MRF) enables fast multiparametric quantitative imaging with a single acquisition and has been shown to improve diagnosis of prostate cancer. However, most prostate MRF studies were performed with spiral acquisitions that are sensitive to B0 inhomogeneities and consequent blurring. In this work, a radial MRF acquisition with a novel subspace reconstruction technique was developed to enable fast T1/T2 mapping in the prostate in under 4 min. The subspace reconstruction exploits the extensive temporal correlations in the MRF dictionary to pre-compute a low dimensional space for the solution and thus reduce the number of radial spokes to accelerate the acquisition. Iterative reconstruction with the subspace model and additional regularization of the signal representation in the subspace is performed to minimize the number of spokes and maintain matching quality and SNR. Reconstruction accuracy was assessed using the ISMRM NIST phantom. In-vivo validation was performed on two healthy subjects and two prostate cancer patients undergoing radiation therapy. The longitudinal repeatability was quantified using the concordance correlation coefficient (CCC) in one of the healthy subjects by repeated scans over 1 year. One prostate cancer patient was scanned at three time points, before initiating therapy and following brachytherapy and external beam radiation. Changes in the T1/T2 maps obtained with the proposed method were quantified. The prostate, peripheral and transitional zones, and visible dominant lesion were delineated for each study, and the statistics and distribution of the quantitative mapping values were analyzed. Significant image quality improvements compared with standard reconstruction methods were obtained with the proposed subspace reconstruction method. A notable decrease in the spread of the T1/T2 values without biasing the estimated mean values was observed with the subspace reconstruction and agreed with reported literature values. The subspace reconstruction enabled visualization of small differences in T1/T2 values in the tumor region within the peripheral zone. Longitudinal imaging of a volunteer subject yielded CCC of 0.89 for MRF T1, and 0.81 for MRF T2 in the prostate gland. Longitudinal imaging of the prostate patient confirmed the feasibility of capturing radiation treatment related changes. This work is a proof-of-concept for a high resolution and fast quantitative mapping using golden-angle radial MRF combined with a subspace reconstruction technique for longitudinal treatment response assessment in subjects undergoing radiation treatment.

1. Introduction

MR fingerprinting (MRF) is a rapid multiparametric quantitative MRI technique that changes the acquisition parameters according to a pre-determined schedule aiming to obtain a unique temporal signal evolution for each set of tissue and system parameters (i.e. T1, T2,

* Corresponding author.
E-mail address: coheno1@mskcc.org (O. Cohen).

https://doi.org/10.1016/j.mri.2023.03.019
Received 1 February 2023; Accepted 29 March 2023
Available online 2 April 2023

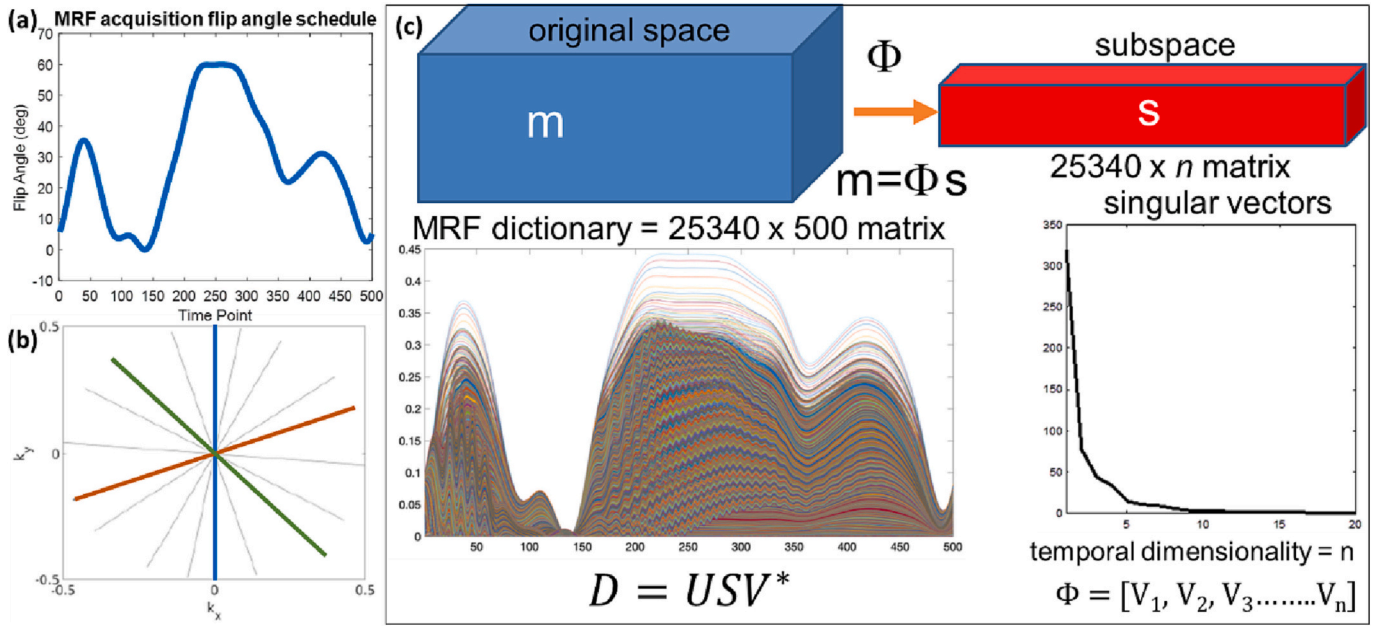

Fig. 1. Components of the proposed method. (a) Flip angle schedule for the MR fingerprinting acquisition with 500 time frames. (b) Radial golden angle readout trajectory with an example of 3 spokes/time frames (different colors indicate different time frames). (c) MRF subspace: The acquired high-dimensional temporal signal m (500 points) can be compressed to a subspace Φ (dimension $n << 500$) by exploiting the structure of the MRF signal. Since the MRF dictionary contains all possible variations of the temporal signal within the defined dictionary parameter value ranges, the temporal subspace Φ can be computed using the first n right singular value vectors of the singular value decomposition of the MRF dictionary entries sorted as a matrix, D = USV*.

diffusion, B0 and B1) [1,2]. MRF has shown promise for measuring tissue changes in pathologies such as cancer [3]. For example, T1 and T2 maps obtained with MRF were shown to improve prostate cancer diagnosis in combination with the apparent diffusion coefficient (ADC) [4–7]. In particular, quantitative T2 maps improved diagnostic power by separating intermediate/high-grade tumors from low-grade tumors [4]. However, longitudinal prostate imaging is challenging due to the deformable and dynamic anatomy of the prostate, its vulnerability to peristaltic motion and bladder filling effects, and distortions due to inherent magnetic susceptibility differences at the interface between different tissues. Most prostate MRF studies to date utilized variable density spiral k-space trajectories [8], which provides fast k-space traversal within a single excitation at the cost of long echo time (TE) and repetition time (TR) and B0-induced blurring.

Radial k-space sampling is an alternative acquisition technique that offers shorter TE/TR to minimize B0 blurring compared to spiral k-space sampling [9,10]. The utilization of the golden-angle acquisition scheme [11], where consecutive spokes are separated by the golden-angle, enables the acquisition of dynamic data with a different uniform k-space coverage in each temporal frame and thus provides enough temporal incoherence for MRF. However, in radial imaging each spoke provides limited k-space coverage, so the acquisition needs to be repeated until a sufficient coverage of k-space in each temporal frame is obtained. Since there are large correlations in the dynamic MRF data and the golden-angle radial acquisition is incoherent, the number of required spokes in each frame can be reduced by compressed sensing techniques [12,13]. A popular technique to accelerate the acquisition of MRF data is to enforce a low-rank condition in the space-time MRF matrix (each temporal frame is a column) [14–16]. Additionally, the MRF dictionary is known to be compressible, and several methods to compress the dictionary based on truncating singular value decomposition have been proposed to improve matching performance [17,18].

Inspired by the subspace reconstruction approach [19], where prior information about a dynamic process is used to build a model with reduced dimensionality (the subspace) and reconstruct undersampled k-space data, this work proposes to build a subspace MRF model using the dictionary entries for reconstruction of undersampled golden-angle radial MRF data. The subspace MRF model is similar to dictionary compression, but the reconstruction algorithm will enforce additional sparsity constraints in the subspace to further increase acceleration and/or improve reconstruction quality. The accuracy of the proposed reconstruction is evaluated in the ISMRM NIST phantom, a multi-compartment phantom with different T1 and T2 relaxation values [20,21]. The in vivo utility of our approach is assessed in healthy subjects and reproducibility is tested by repeated scans over the course of a year. The potential use of the method for longitudinal treatment response assessment is demonstrated in a patient with prostate cancer undergoing high dose rate brachytherapy and external beam radiation therapy treatments.

2. Methods

2.1. Radial MR fingerprinting sequence

A multi-slice gradient-spoiled steady-state-free-precession (SSFP) MRF sequence with inversion preparation was used with golden angle radial trajectory readout [22] on a clinical 3 T scanner (Ingenia Elition X, Philips Healthcare, Best, The Netherlands). A 28-channel combined anterior and posterior receiver coil elements was used. MRF acquisition parameters are as follows: FOV = 250 × 250 mm^2, image matrix = 224 × 224 (in-plane resolution of 1.1 mm), slice thickness = 5 mm, number of slices = 15, TE = 4 ms, TR = 10 ms, variable flip angle range = 0–60 degrees. The acquisition schedule contains 500 time frames, as shown in Fig. 1a. An example of the radial golden angle readout trajectory for 3 spokes/time frames is shown in bold in Fig. 1b. For all studies, scans with 3 and 5 radial spokes per time frame were performed, with scan times of 3:47 min and 6:18 min, respectively. The goal of these experiments was to test the feasibility of quantitative mapping with a scan time lower than 4 min. The T1 and T2 value ranges for the utilized MRF dictionary were 1–5000 ms and 1–3000 ms, respectively. Dictionary resolutions for T1 values were defined as [1:2:99, logspace(2, 3.5, p = 180), 3000:500:5000], and for T2 values were defined as [1:2:99,

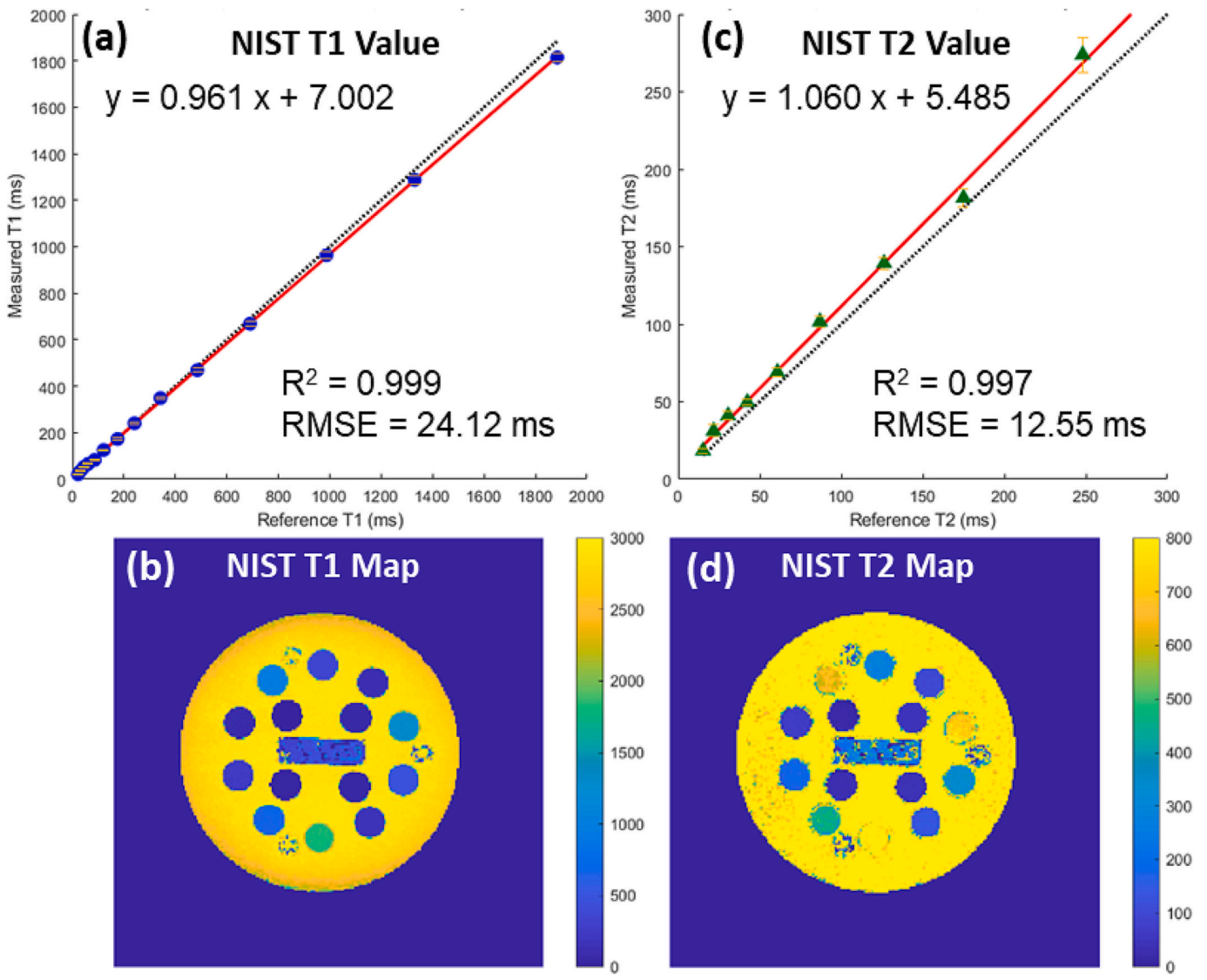

Fig. 2. Comparison between the estimated and reference values in the NIST phantom. (a) Estimated T1 values plotted against reference values and (b) associated T1 map. (c) Estimated T2 values plotted against reference values and (d) associated T2 map.

logspace(2, 3, p = 120), 1500:500:3000], denoted by min:increment: max and logspace(a, b, p) = p logarithmically spaced points in the range of 10^a and 10^b. The full dictionary contained 25,340 entries which were corrected for slice profile imperfections [23].

2.2. Subspace reconstruction and parameter selection

Since the entries of the MRF dictionary are highly correlated and contain all possible variations of the temporal signal within the defined dictionary parameter value ranges, a temporal subspace can be estimated to constrain the reconstruction of the series of undersampled temporal frames (Fig. 1c). The temporal subspace Φ is computed using the first n right singular value vectors of the singular value decomposition of the MRF dictionary entries sorted as a matrix, D = USV*. The high-dimensional time-series m (500 temporal frames) can be projected into the subspace $\boldsymbol{s} = \Phi^* m$, where $\boldsymbol{s}$ is the low-dimensional representation of m. Generally, the number of k-space data samples required for accurate reconstruction is determined by the sparsity in the image or in a transform domain [24] and since $\boldsymbol{s}$ has lower dimensionality, it will require fewer k-space radial lines for each time frame. In addition, sparsity constraints will be applied on $\boldsymbol{s}$ to maximize SNR. Subspace MRF reconstruction is performed by solving the following optimization problem:

$$\underset{s}{\operatorname{argmin}} \frac{1}{2}\|\boldsymbol{E\Phi s} - \boldsymbol{d}\|_2^2 + \lambda\|\boldsymbol{Ts}\|_1,$$

where $\boldsymbol{E}$ represents the acquisition operator, $\boldsymbol{d}$ = time-series k-space data, $\boldsymbol{T}$ is a first-order difference operator that will minimize total variation among the entries of $\boldsymbol{s}$ for additional regularization and λ is the weighting factor for the additional regularization in the subspace. The reconstruction was implemented in MATLAB (Natick, Massachusetts, USA) using a non-linear conjugate gradient algorithm[13].

Two parameters influenced the subspace reconstruction performance: (1) number of singular vectors used in the subspace dictionary time dimension, n, and (2) the weighting factor λ. To find the optimal combination of reconstruction parameters, an exhaustive search was performed for n ranging from 5 to 15 and λ from 0.005 to 0.1 in increments of 0.001 with both a 3 spokes/time frame and 5 spokes/time frame scan on the ISMRM NIST phantom [21]. The combination of parameter values resulting in the lowest combined T1/T2 root-mean-square-error (RMSE) values relative to the reference values were selected.

To evaluate the image quality improvements due to the MRF

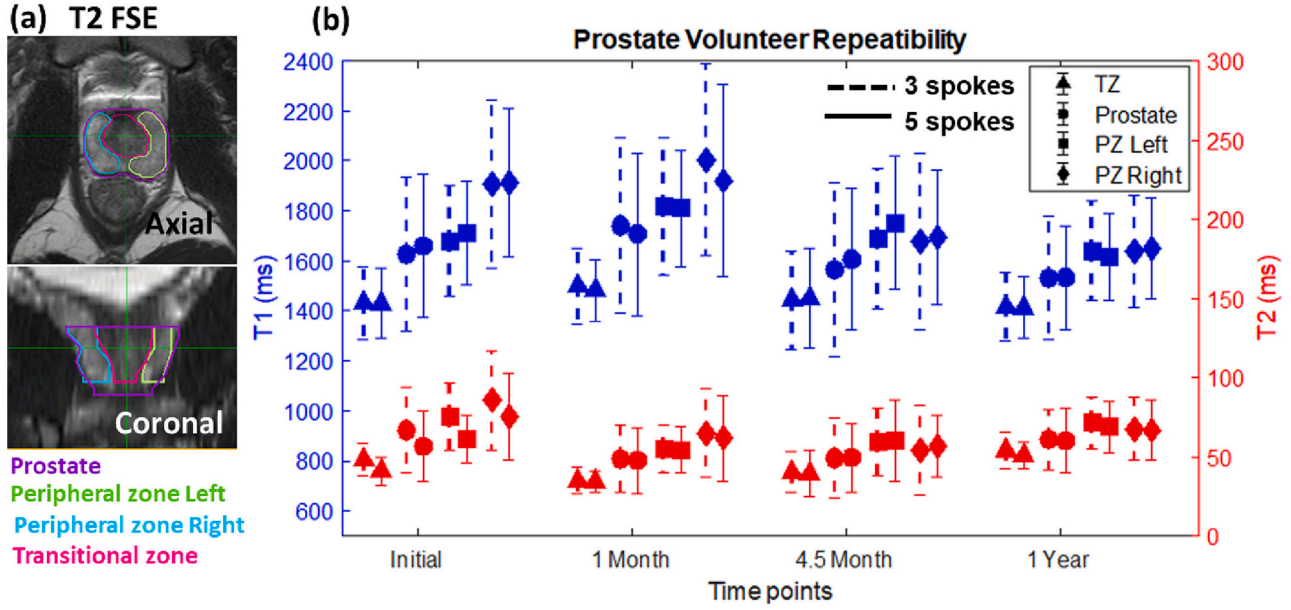

Fig. 3. Estimated T1/T2 values in a healthy subject for the acquisitions with 3 and 5 spokes per time frame across different time points. (a) ROIs defined on axial and coronal T2-weighted anatomical images. (b) Mean ± SD of the T1 and T2 values obtained with the 3 spoke (dashed) and 5 spoke (solid) acquisitions. TZ: transitional zone (triangle), PZ: peripheral zone (left: square, right: diamond), prostate gland (circle).

subspace reconstruction, standard nonuniform Fourier transform (NUFFT) reconstruction [25] as well as a golden-angle radial sparse parallel (GRASP) reconstruction method [12] were also performed, and the resultant T1 and T2 parameter maps were compared. In all cases, T1 and T2 relaxation parameter maps were calculated by pattern-matching the measured signal to the simulated MRF dictionary. For NUFFT reconstruction, matching was performed on a temporally compressed dictionary, as previously described [26], using 25 singular vectors. Acquisitions with 3 and 5 radial spokes per time frame were performed for all studies.

2.3. Phantom validation

The radial MRF sequence and proposed MRF subspace reconstruction pipeline was tested in the ISMRM NIST phantom. Regions-of-interest (ROIs) were drawn around each compartment and the mean and standard deviation (SD) calculated and compared to the reference values for T1/T2 ranges relevant to prostate imaging. The reference values provided by the phantom manufacturer were obtained using gold-standard spectroscopic inversion-recovery and spin-echo sequences [21]. The RMSE and Pearson correlation coefficient between the estimated and reference values were calculated for T1 and T2.

2.4. In-vivo studies

2.4.1. Healthy subjects

Two healthy volunteers (ages 37 and 39) were recruited to this study and gave informed Institutional Review Board consent. To quantify the repeatability of the proposed sequence for longitudinal response assessments, repeated acquisitions at four different time points (initial, 1 month, 4.5 months, and 1 year) were performed on one of the subjects. An axial T2-weighted 2D fast spin echo (FSE) scan was also acquired for anatomical definitions. All scans were co-registered using MIM Vista™ (MIM Software Inc., Cleveland, OH, USA). ROIs defining the peripheral zone (PZ), transitional zone (TZ), and the whole prostate gland were made using the T2-weighted scan from the first time point, and transferred to the other time points through rigid image registration [27]. The statistics and distribution of the quantitative values (T1 and T2) were analyzed for all defined ROIs. The Lin's concordance correlation coefficient [28] (CCC) was calculated in all defined ROIs as a measure of the reproducibility of each parameter. The quantified T1 and T2 values in the second healthy subject was compared to that of the first subject.

2.4.2. Patient studies

Two patients with biopsy-proven adenocarcinoma of the prostate and at least 1 dominant MRI-visible lesion were recruited for this study and gave informed Institutional Review Board consent. Patient 1 (age: 74) has a biochemically recurrent prostate adenocarcinoma with a 2.8 cm bilateral posterior base to apex peripheral zone lesion suspicious for residual/recurrent tumor with potentially residual extracapsular extension abutting the anterior rectal wall. The patient had received prior radiation therapy 9 years prior to the one imaging study that was performed after rectal spacer and gold seed fiducial placement prior to external beam radiation therapy.

Patient 2 (age: 64) has a 1.4 cm lesion involving the anterior apex of the transitional zone without extracapsular extension. Three scans were performed on this patient to assess longitudinal imaging changes: an initial pretreatment scan, a second scan following a single fraction Ir-192 high dose rate brachytherapy treatment of 15 Gy in additional to rectal spacer and gold seed fiducial marker placement, and a third scan 3 months after completion of external radiation therapy of 25 Gy in 5 fractions to the prostate.

Both patients were scanned with the institutional standard-of-care protocol which included T2-weighted and DWI imaging as well as with the proposed MRF pulse sequence.

For analysis, ROI contours were created for the prostate gland, non-tumor transitional zone and peripheral zone, as well as gold seed fiducials by a trained medical physicist (V.Y.). Dominant lesion contours delineated by trained radiation oncologists (M.Z., D.S.) were used for analysis of the tumor. The gold seed fiducial markers were excluded from ROI analysis with a 2 mm uniform expansion around the fiducial marker contours created.

3. Results

3.1. Phantom validation

The mean ± SD of the T1 and T2 values in the phantom obtained

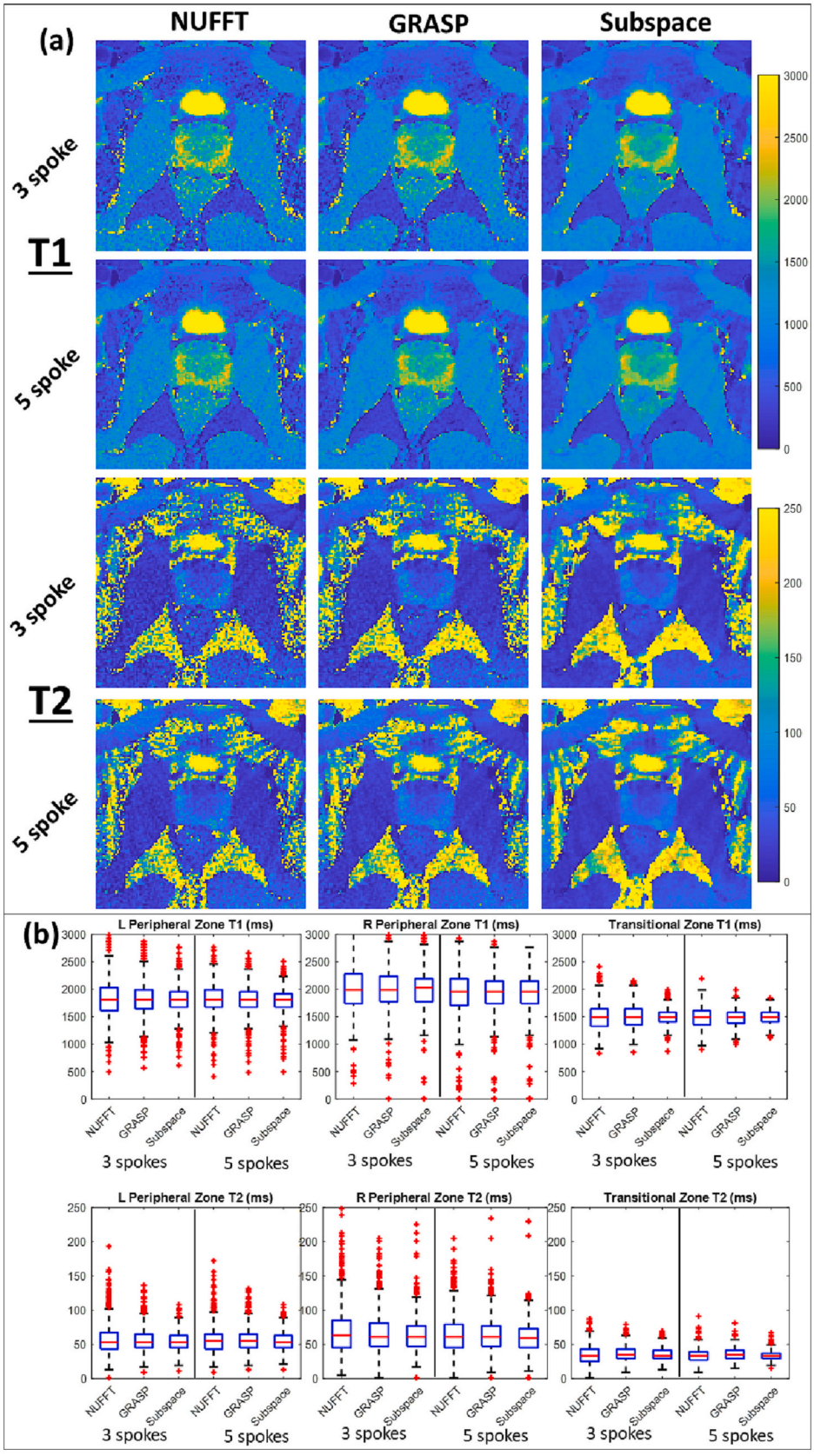

Fig. 4. Comparison between tissue maps obtained with the different reconstruction methods. (a) T1 and T2 maps obtained with the NUFFT, GRASP, and Subspace reconstructions for both acquisitions with 3 and 5 spokes. (b) Boxplots of the distribution of T1 and T2 values in the evaluated ROIs.

Table 1
Representative estimated T1 and T2 values (mean ± SD) for all reconstruction methods from the second time point of healthy subject 1. (a) acquisition with 3 spokes per time frame (b) acquisition with 5 spokes per time frame (c) concordance correlation coefficient and corresponding 95% confidence interval across all four time points for the subspace reconstruction from the data acquired with 5 spokes.

	T1 (ms) μ ± σ			T2 (ms) μ ± σ		
	NUFFT	GRASP	Subspace	NUFFT	GRASP	Subspace
(a) 3 spokes/time frame						
PZ Left	1825.1 ± 351.0	1821.0 ± 311.2	1815.7 ± 274.4	57.7 ± 23.5	56.6 ± 18.5	54.7 ± 14.9
PZ Right	2019.1 ± 455.5	2008.6 ± 415.5	2003.1 ± 384.6	77.0 ± 124.8	68.8 ± 40.3	64.9 ± 27.8
TZ	1496.9 ± 243.4	1497.4 ± 203.5	1498.3 ± 151.3	35.3 ± 13.6	36.1 ± 10.9	34.8 ± 8.6
Prostate	1748.2 ± 418.4	1746.0 ± 385.9	1739.6 ± 350.9	53.4 ± 65.2	50.9 ± 27.4	48.6 ± 21.4
(b) 5 spokes/time frame						
PZ Left	1827.6 ± 293.8	1818.7 ± 263.8	1810.2 ± 231.1	56.9 ± 20.9	56.5 ± 17.6	54.4 ± 14.4
PZ Right	1932.6 ± 412.1	1927.0 ± 391.0	1920.5 ± 383.7	65.8 ± 36.7	64.6 ± 29.9	61.9 ± 27.1
TZ	1479.8 ± 185.6	1481.1 ± 157.7	1482.2 ± 125.0	34.4 ± 9.8	35.4 ± 8.2	34.3 ± 6.4
Prostate	1714.8 ± 367.4	1712.0 ± 343.0	1708.1 ± 325.1	49.8 ± 28.3	49.5 ± 23.8	47.5 ± 20.6

(c) Concordance correlation coefficient (CCC) across four time points (5 spokes/time frame)

	T1 subspace		T2 subspace	
	CCC	95% CI	CCC	95% CI
PZ Left	0.872	[0.865, 0.878]	0.901	[0.890, 0.911]
PZ Right	0.870	[0.864, 0.877]	0.746	[0.716, 0.773]
TZ	0.889	[0.883, 0.894]	0.677	[0.652, 0.700]
Prostate	0.890	[0.884, 0.895]	0.816	[0.805, 0.826]

from the proposed method is shown in Fig. 2a and c, respectively. The corresponding T1 and T2 maps are shown in Fig. 2b and d. Both T1 and T2 values were strongly correlated ($R^2 = 0.99$) with the reference values, with RMSE values of 24.12 ms for T1 and 12.55 ms for T2. The equations of the best-fit lines to the data showed little deviation from linearity for both T1 (3.9%) and T2 (6.0%) and minimal bias of 7.0 ms and 5.5 ms for T1 and T2, respectively. The exhaustive search for the optimal reconstruction parameters yielded a value of $\lambda = 0.005$ and $n = 9$ singular values for acquisitions with 3 spokes (scan time = 3:47 min) and $\lambda = 0.005$ and $n = 7$ for acquisitions with 5 spokes (scan time = 6:18 min).

3.2. In-vivo studies

3.2.1. Healthy subjects

The ROIs used in the repeatability analysis were drawn on a T2-weighted scan (Fig. 3a). The mean ± SD of the T1 and T2 values in each ROI for all four time points for the acquisitions with 3 spokes and 5 spokes per time frame are shown in Fig. 3b. The acquisition with 3 spokes per time frame is represented with a dashed error bar, and the one with 5 spokes per time frame with a solid error bar. Fig. 4a and b shows a comparison between the T1 and T2 maps obtained with the NUFFT, GRASP, and proposed subspace reconstructions and the distribution of values for each method in boxplot format. The mean ± SD values for all evaluated regions in the second time point, as an example, are also tabulated in Table 1. The CCC for right and left PZ, TZ, and prostate gland for the proposed subspace reconstruction are shown in Table 1.

Results obtained from the second volunteer subject yielded T1/T2 (μ ± σ) values of 1761.6 ± 216.4/70.3 ± 16.9 ms in the PZ, and 1541 ± 224.2/56.8 ± 13.21 ms in the TZ. As compared to values presented in Table 1 from volunteer 1, the obtained PZ average T1 and T2 values in volunteer 2 are 48.5 ms higher and 15.87 ms lower than that of volunteer 1. For the TZ, the mean T1 and T2 values were 59.1 ms higher and 22.5 ms lower compared to volunteer 1, respectively. The image quality is similar to that of volunteer subject 1.

3.2.2. Patient studies

The T1 and T2 maps obtained with the different reconstruction methods are shown in Fig. 5a along with T2-weighted and ADC images in patient 1 who had undergone a scan prior to external beam radiation therapy treatments. The subspace-reconstructed maps were less noisy than the NUFFT or GRASP reconstructions contributing to the smaller spread evident in the boxplot shown in Fig. 5b. A subtle decrease in T1 values in the tumor region compared with surrounding tissue is seen on both the T1 map and the ROI values.

Figure 6a shows the MRF T1 and T2 maps, as well T2-weighted and diffusion-weighted image for the second patient for all three time points. Fig. 6b demonstrates the evaluated ROIs, and Fig. 6c plots the time progression of the mean T1 and T2 values obtained with the proposed subspace reconstruction using a 5 spoke/time frame in the lesion, PZ, and TZ regions. The T1 and T2 values for all time points and acquisitions are tabulated in Table 2.

4. Discussion

4.1. Comparison with previous radial MRF techniques

This study demonstrates a novel subspace MRF reconstruction method that exploits the temporal compression of the dictionary to constrain an iterative reconstruction and highly accelerate the acquisition of radial MRF data. The short readout of radial trajectories reduces sensitivity to B0 inhomogeneities compared to spiral or EPI trajectories, but the acquisition needs to be repeated to obtain sufficient k-space coverage. Several techniques were previously developed to exploit correlations in the data and reduce the number of spokes, including compressed sensing and low-rank reconstruction [9,14,29]. However, previous work exploited implicit sparsity or low-rankness in the time-series of images or constrained the space of the solution separately. This work combined both ideas and simultaneously constrained the space of the solution to a lower dimensional space given by MRF dictionary compression and applied additional regularization on the subspace signal representation. The latter was particularly important to reduce variability in the fitting process and increase SNR in the reconstructed T1 and T2 maps. Another innovation is the clinical application to longitudinal imaging of prostate cancer. As overall survival of cancer patients improves due to advances in treatment management [30], longitudinal monitoring of these patients gains importance. To our knowledge, this is the first demonstration of long-term (1 year) longitudinal MRF imaging of the prostate.

4.2. Comparison with previous prostate MRF studies

A recent prostate MRF study in 84 patients reported normal peripheral zone (NPZ) T1 and T2 values of 2240 ± 360 ms and 146 ± 61 ms, and non-cancerous tissues and benign prostatic tissue T1 and T2 values of 1790 ± 290 ms, and 73 ± 37 ms [6]. The NPZ T1 (1920.5 ± 383.7 ms) and T2 (61.9 ± 27.1 ms) values obtained in our study were somewhat lower. This may be due to differences in the ROI selection approach used in each study. Previous studies defined the NPZ ROIs by selecting hyperintense values directly on the MRF maps thereby biasing the tissue means towards higher values. This study used the PI-RADS sector map [31] and T2-weighted scans to define the general peripheral zone region and other ROIs. This provided more consistent

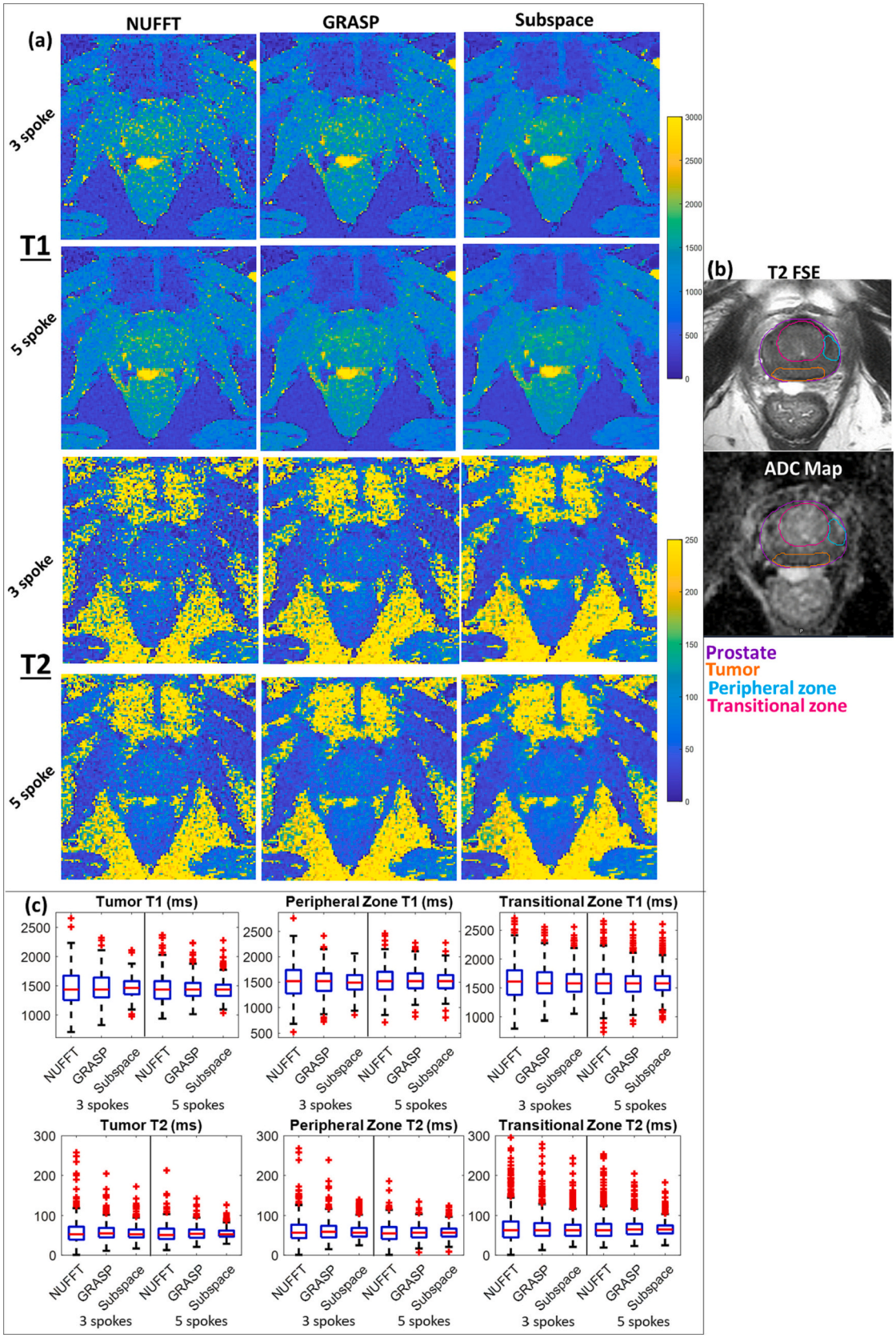

Fig. 5. Tissue maps for patient 1 (74-year old) with a 2.8 cm bilateral posterior base to apex peripheral zone lesion. (a) T1 and T2 maps for the NUFFT, GRASP, and Subspace reconstructions for the 3- and 5- spoke per time frame, (b) utilized ROIs as defined on T2-weighted imaging and diffusion maps, and (c) boxplots demonstrating the distribution of T1 and T2 values in evaluated ROIs for both acquisitions (3 and 5 spokes per time frame) and all tested reconstruction methods.

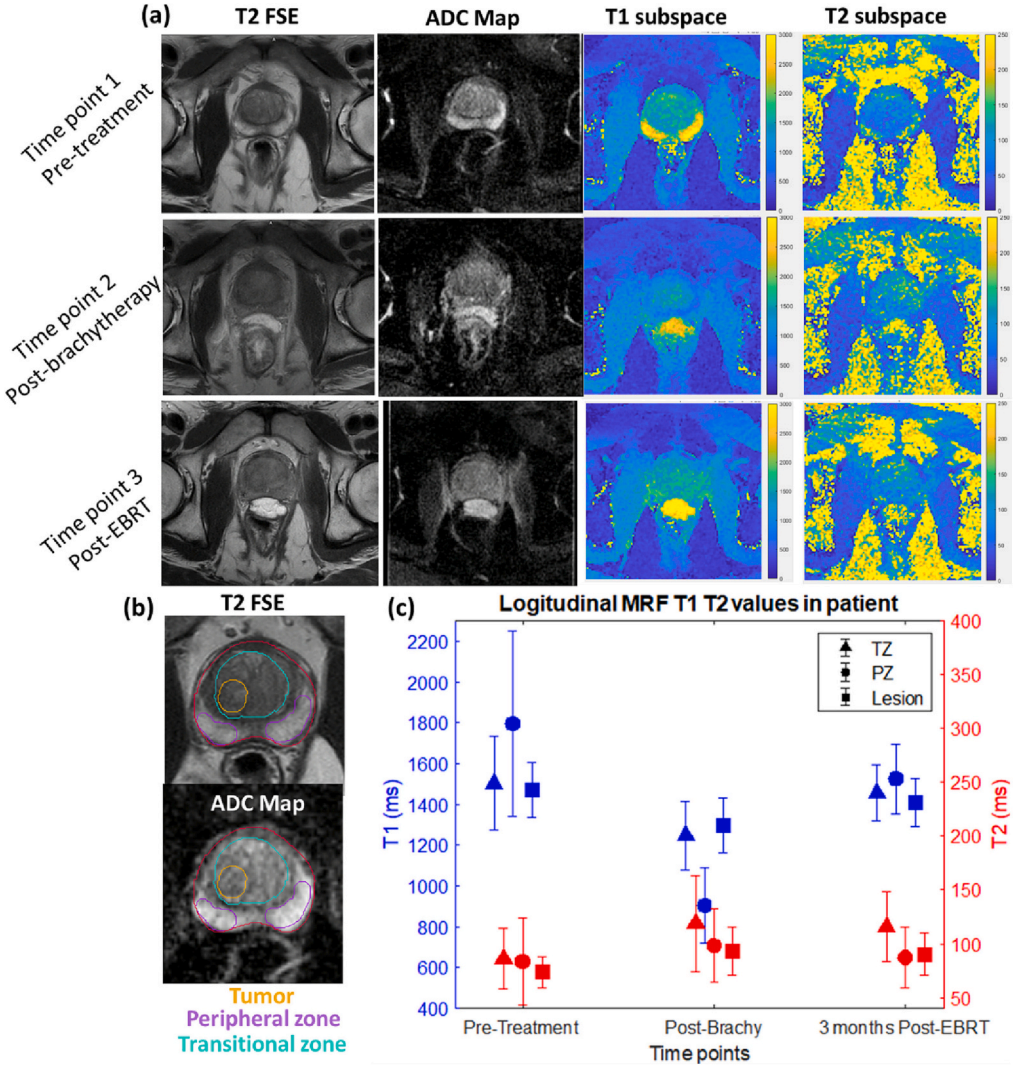

Fig. 6. Tissue maps obtained from patient 2 (64-year old) with a 1.4 cm lesion involving the anterior apex of the transitional zone without extracapsular extension. (a) T2-weighted imaging, ADC maps, T1/T2 maps acquired with subspace reconstruction for all three time points (b) contour definition of tumor, PZ, and TZ overlaid on T2 FSE and ADC maps from the pre-treatment time point. (c) The mean ± SD T1 and T2 values in each region plotted over time to demonstrate longitudinal changes following two types of radiation treatments.

Table 2
Progression of the mean ± SD of the T1 and T2 values for all time points (tp 1, tp2, and tp3) and all reconstruction methods evaluated. TZ = transitional zone, PZ = peripheral zone.

		T1 (ms) μ ± σ			T2 (ms) μ ± σ		
		NUFFT	GRASP	Subspace	NUFFT	GRASP	Subspace
(a) 3 spokes/time frame							
	TZ	1508.4 ± 325.7	1501.2 ± 269.7	1510.3 ± 244.8	101.7 ± 96.1	94.4 ± 41.9	90.3 ± 35.1
tp1	Lesion	1448.8 ± 235.5	1448.3 ± 182.8	1455.8 ± 167.4	79.7 ± 38.2	78.0 ± 27.0	74.1 ± 21.1
	PZ	1659.4 ± 492.9	1659.8 ± 444.6	1669.4 ± 429.3	94.0 ± 166.0	79.7 ± 45.8	75.8 ± 39.5
	TZ	1338.8 ± 268.2	1332.6 ± 217.9	1341.1 ± 178.0	127.2 ± 99.2	118.4 ± 54.0	112.2 ± 42.6
tp2	Lesion	1361.3 ± 242.2	1351.5 ± 187.2	1356.9 ± 133.5	102.6 ± 52.5	98.3 ± 36.2	93.6 ± 28.5
	PZ	971.9 ± 290.5	968.4 ± 252.6	967.1 ± 228.3	104.0 ± 85.9	97.8 ± 44.3	92.9 ± 35.4
	TZ	1462.1 ± 287.8	1458.4 ± 242.9	1468.4 ± 173.4	159.4 ± 156.8	147.3 ± 98.0	130.0 ± 46.9
tp3	Lesion	1481.7 ± 258.7	1485.0 ± 219.2	1502.8 ± 146.8	127.7 ± 77.3	123.4 ± 52.9	113.8 ± 28.8
	PZ	1475.4 ± 342.3	1472.2 ± 281.0	1479.7 ± 184.7	123.6 ± 149.8	110.6 ± 81.5	97.1 ± 32.0
(b) 5 spokes/time frame							
	TZ	1493.6 ± 276.1	1492.3 ± 235.7	1503.6 ± 230.8	90.6 ± 41.7	89.7 ± 30.4	86.0 ± 28.0
tp1	Lesion	1456.7 ± 200.4	1451.7 ± 157.5	1472.4 ± 134.5	77.0 ± 21.8	76.9 ± 16.2	73.8 ± 14.5
	PZ	1778.5 ± 495.0	1775.1 ± 451.5	1796.0 ± 453.3	92.3 ± 109.0	87.3 ± 45.5	83.6 ± 40.5
	TZ	1241.6 ± 215.5	1238.7 ± 179.2	1247.6 ± 168.1	127.3 ± 70.0	123.0 ± 48.5	118.7 ± 44.7
tp2	Lesion	1285.8 ± 197.9	1283.4 ± 154.2	1298.6 ± 135.1	99.2 ± 39.1	97.4 ± 25.6	93.2 ± 21.9
	PZ	898.0 ± 215.9	899.0 ± 189.2	904.5 ± 186.8	104.5 ± 49.9	101.6 ± 34.9	98.4 ± 33.6
	TZ	1445.9 ± 213.4	1446.6 ± 176.9	1456.1 ± 135.9	125.9 ± 74.4	122.8 ± 44.9	115.7 ± 32.2
tp3	Lesion	1399.8 ± 213.5	1398.4 ± 170.2	1408.0 ± 117.1	96.3 ± 38.0	95.5 ± 28.5	90.4 ± 19.7
	PZ	1517.0 ± 270.7	1516.1 ± 222.0	1524.6 ± 171.4	101.0 ± 83.0	95.4 ± 45.2	87.3 ± 27.9

longitudinal ROIs across multiple time points. However, some regions defined as normal benign prostatic tissue on the MRF maps may have been included in the NPZ ROIs in this study, which would lower the estimated T1/T2 values. The range of estimated T1/T2 values with our method in the healthy subjects (T1 = 1647–1920 ms, T2 = 54.4–75.2 ms) was between the reported ranges of NPZ and non-cancerous/benign prostatic tissues [6], which supports this assessment.

The long-term repeatability of the proposed method in a healthy subject over the span of one year was appropriate, as shown in Fig. 3b. Different regions were evaluated with CCC values ranging from 0.87 to 0.89 for T1 and 0.67–0.90 for T2. The lower repeatability in comparison to other studies [32] can be attributed to several factors. First, repeatability analysis is typically performed on consecutive scans within a short period of time [32], whereas in this study the four scans were performed over the span of one year. Although consecutive scans mitigate biological variations between scans, they don't accurately reflect long-term imaging typical of cancer management. Relatedly, positional shifts in the prostate may have resulted in imperfect co-registration between scans reducing the correlation between the ROIs tested. The prostate is a deformable organ, and the relative positioning of the prostate gland is readily influenced by the surrounding organs like the bladder. As an example, imaging changes of 12% have been reported in the peripheral zone based on the timing of previous ejaculation [33]. Similarly, rectal spacers, gold fiducial marker implants or invasive needle incisions used in high dose rate brachytherapy treatments may also affect the prostate positioning and hence T1 and T2 reproducibility across time points. Variations in prostate T1/T2 values are therefore to be expected and can be addressed with improved image registration algorithms [34] and volumetric acquisitions that will be studied in future work.

4.3. Treatment-related changes on tissue maps

The MRF maps and temporal signal plots presented clear treatment-related changes for patient 2. Specifically, a substantial reduction in T1 values in the peripheral zone, and loss in separation between the peripheral zone and transitional zone during the second time point was observed, followed by a modest recovery at the final post treatment time point that did not reach the pre-treatment levels. The imaging changes observed were consistent with radiation-induced glandular loss and fibrosis resulting in loss of differentiation between the TZ and PZ on MRI, and leading to diffuse and low signal intensity on T2-weighted imaging [35]. It is also interesting to note that the T1 value of the lesion was slightly lower than that of the surrounding transitional zone prior to treatment and after treatment, but for the middle time point, the lesion appears to have slightly higher values than that of surrounding transitional zone tissue. This change in relative values between tumor and surrounding transitional zone could indicate transient tissue changes occurring in response to the brachytherapy radiation treatment [35]. A reduction in SD and spread from the subspace reconstruction is still seen.

4.4. Limitations and future work

This study has a few limitations. The number of in-vivo subjects included in this study (2 healthy subjects and 2 patients) was relatively small but sufficient to demonstrate the benefits of the proposed subspace reconstruction method. To our knowledge, this is the first study that quantifies longitudinal radiation-treatment related changes with MRF quantitative tissue mapping. Streaking flow artifacts originating from the nearby large vessels were observed in some subjects. In most scans the artifacts do not traverse into the prostate region but may influence the overall quality of the image. Given the variability in patient anatomies, determining the impact of these artifacts prior to scanning is challenging. Flow mitigation strategies using gradient moment nulling have been demonstrated for spiral MRF in the prostate [36], and could be applied in our method as well albeit at the cost of slightly increased echo time. This will be investigated in future work. The reconstruction parameters (λ, n) used in this work were obtained using phantom experiments. However, prostate-specific regularization parameters may provide higher quality tissue parameter maps and will be investigated in future studies.

5. Conclusion

This work demonstrated the feasibility of fast high-resolution T1 and T2 mapping using golden-angle radial MRF and a novel subspace reconstruction technique that combines MRF dictionary compression and subspace regularization. This approach not only significantly improves image quality compared with standard reconstruction methods, but also enables substantial shortening of scan time by 40% without sacrificing image quality and parameter mapping accuracy. Future work will focus on a larger patient population, patient-specific image quality variations and analysis of different treatment related changes that can be captured by the proposed method.

Author contributions

VY, RO, and OC conceptualized the study. MB, PK, PM and MD contributed to the implementation of the pulse sequence. RO and OC contributed to the algorithm design. DS and MZ contributed to patient recruitment and tumor delineations. VY, CW and ES performed data collection and analysis. VY, RO, CW, ES, MB, PK, MD, PM, DS, MZ, LC and OC wrote and/or substantially revised the manuscript.

Funding

This work was partially supported by Philips Healthcare and NIH/NCI grants R37CA262662 and P30-CA008748. The content is solely the responsibility of the authors and does not necessarily represent the official views of the National Institutes of Health.

Declaration of Competing Interest

This work was performed as part of a master research agreement between MSKCC and Philips Healthcare. MB, MD, PM, and PK were employees of Philips Healthcare while making contributions to this work.

Acknowledgement

This work was performed in collaboration with Philips Healthcare as part of a master research agreement. The authors would like to thank Dr. Ramin Jafari for his technical assistance on the pulse sequence implementation, and the MRI technologists and therapists in Memorial Sloan Kettering Cancer Center Department of Radiation Oncology for their skilled assistance in patient and volunteer subject data acquisitions.

References

[1] Ma D, et al. Magnetic resonance fingerprinting. Nature 2013;495(7440):187–92.
[2] Jiang Y, Ma D, Seiberlich N, Gulani V, Griswold MA. MR fingerprinting using fast imaging with steady state precession (FISP) with spiral readout. Magn Reson Med 2015;74(6):1621–31.
[3] Poorman ME, et al. Magnetic resonance fingerprinting part 1: potential uses, current challenges, and recommendations. J Magn Reson Imaging 2020;51(3):675–92.
[4] Yu AC, et al. Development of a combined MR fingerprinting and diffusion examination for prostate cancer. Radiology 2017;283(3):729–38.
[5] Sushentsev N, et al. The effect of gadolinium-based contrast agent administration on magnetic resonance fingerprinting-based T1 relaxometry in patients with prostate cancer. Sci Rep 2020;10(1):20475.
[6] Panda A, et al. Targeted biopsy validation of peripheral zone prostate cancer characterization with MR fingerprinting and diffusion mapping. Investig Radiol 2019;54(8):485.

[7] Panda A, et al. MR fingerprinting and ADC mapping for characterization of lesions in the transition zone of the prostate gland. Radiology 2019;292(3):685–94.
[8] Lo W-C, Panda A, Jiang Y, Ahad J, Gulani V, Seiberlich N. MR fingerprinting of the prostate. MAGMA 2022;35(4):557–71.
[9] Ehses P, et al. IR TrueFISP with a golden-ratio-based radial readout: fast quantification of T1, T2, and proton density. Magn Reson Med 2013;69(1):71–81.
[10] Feng L. Golden-angle radial MRI: basics, advances, and applications. J Magn Reson Imaging 2022;56(1):45–62.
[11] Winkelmann S, Schaeffter T, Koehler T, Eggers H, Doessel O. An optimal radial profile order based on the Golden ratio for time-resolved MRI. IEEE Trans Med Imaging 2006;26(1):68–76.
[12] Feng L, et al. Golden-angle radial sparse parallel MRI: combination of compressed sensing, parallel imaging, and golden-angle radial sampling for fast and flexible dynamic volumetric MRI. Magn Reson Med 2014;72(3):707–17.
[13] Lustig M, Donoho D, Pauly JM. Sparse MRI: the application of compressed sensing for rapid MR imaging. Magnet Reson Med: Off J Intern Soc Magnet Reson Med 2007;58(6):1182–95.
[14] Lima da Cruz G, Bustin A, Jaubert O, Schneider T, Botnar RM, Prieto C. Sparsity and locally low rank regularization for MR fingerprinting. Magn Reson Med 2019;81(6):3530–43.
[15] Mazor G, Weizman L, Tal A, Eldar YC. Low-rank magnetic resonance fingerprinting. Med Phys 2018;45(9):4066–84.
[16] Assländer J, Cloos MA, Knoll F, Sodickson DK, Hennig J, Lattanzi R. Low rank alternating direction method of multipliers reconstruction for MR fingerprinting. Magn Reson Med 2018;79(1):83–96.
[17] Cauley SF, et al. Fast group matching for MR fingerprinting reconstruction. Magn Reson Med 2015;74(2):523–8.
[18] Yang M, et al. Low rank approximation methods for MR fingerprinting with large scale dictionaries. Magn Reson Med 2018;79(4):2392–400.
[19] Christodoulou AG, Hitchens TK, Wu YL, Ho C, Liang Z-P. Improved subspace estimation for low-rank model-based accelerated cardiac imaging. IEEE Trans Biomed Eng 2014;61(9):2451–7.
[20] Jiang Y, Ma D, Keenan KE, Stupic KF, Gulani V, Griswold MA. Repeatability of magnetic resonance fingerprinting T1 and T2 estimates assessed using the ISMRM/NIST MRI system phantom. Magn Reson Med 2017;78(4):1452–7.
[21] Stupic KF, et al. A standard system phantom for magnetic resonance imaging. Magn Reson Med 2021;86(3):1194–211.
[22] Li Z, Berman BP, Galons J-P, Bilgin A, Altbach MI, Martin DR. Rapid high-resolution T1 mapping using highly accelerated radial steady-state free-precession acquisition. In: Proceedings of the 24th Annual Meeting of ISMRM, Singapore; 2016. p. 4196.
[23] Ma D, et al. Slice profile and B1 corrections in 2D magnetic resonance fingerprinting. Magn Reson Med 2017;78(5):1781–9.
[24] Otazo R, Kim D, Axel L, Sodickson DK. Combination of compressed sensing and parallel imaging for highly accelerated first-pass cardiac perfusion MRI. Magn Reson Med 2010;64(3):767–76.
[25] Fessler JA, Sutton BP. Nonuniform fast Fourier transforms using min-max interpolation. IEEE Trans Signal Process 2003;51(2):560–74.
[26] McGivney DF, et al. SVD compression for magnetic resonance fingerprinting in the time domain. IEEE Trans Med Imaging 2014;33(12):2311–22.
[27] Hill DL, Batchelor PG, Holden M, Hawkes DJ. Medical image registration. Phys Med Biol 2001;46(3):R1.
[28] Lawrence I, Lin K. A concordance correlation coefficient to evaluate reproducibility. Biometrics 1989:255–68.
[29] Cloos MA, et al. Rapid radial T1 and T2 mapping of the hip articular cartilage with magnetic resonance fingerprinting. J Magn Reson Imaging 2019;50(3):810–5.
[30] Miller KD, et al. Cancer treatment and survivorship statistics, 2022. CA Cancer J Clin 2022;72(5):409–36.
[31] Weinreb JC, et al. PI-RADS prostate imaging–reporting and data system: 2015, version 2. Eur Urol 2016;69(1):16–40.
[32] Lo W-C, et al. Multicenter repeatability and reproducibility of MR fingerprinting in phantoms and in prostatic tissue. Magn Reson Med 2022;88(4):1818–27.
[33] Medved M, Sammet S, Yousuf A, Oto A. MR imaging of the prostate and adjacent anatomic structures before, during, and after ejaculation: qualitative and quantitative evaluation. Radiology 2014;271(2):452–60.
[34] Klein S, Staring M, Murphy K, Viergever MA, Pluim JP. Elastix: a toolbox for intensity-based medical image registration. IEEE Trans Med Imaging 2009;29(1):196–205.
[35] Patel P, Mathew MS, Trilisky I, Oto A. Multiparametric MR imaging of the prostate after treatment of prostate cancer. Radiographics 2018;38(2):437–49.
[36] Baumann M, et al. Towards A clinical prostate MR fingerprinting protocol. In: Proceedings of the International Society of Magnetic Resonance in Medicine, London; May 2022. p. 2593.